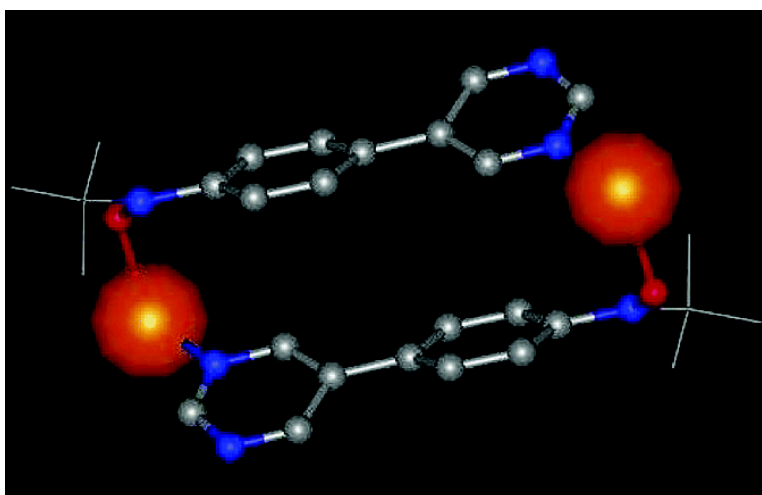Article

Manganese(II) and Copper(II) Hexafluoroacetylacetonate 1:1 Complexes with 5-(4-[*N-tert*-Butyl-*N*-aminoxyl]phenyl)pyrimidine: Regiochemical Parity Analysis for Exchange Behavior of Complexes between Radicals and Paramagnetic Cations

Lora M. Field, Paul M. Lahti, Fernando Palacio, and Armando Paduan-Filho

More About This Article

Additional resources and features associated with this article are available within the HTML version:

- Supporting Information
- Links to the 1 articles that cite this article, as of the time of this article download
- Access to high resolution figures
- Links to articles and content related to this article
- Copyright permission to reproduce figures and/or text from this article

View the Full Text HTML

Manganese(II) and Copper(II) Hexafluoroacetylacetonate 1:1 Complexes with 5-(4-[*N-tert*-Butyl-*N*-aminoxyl]phenyl)pyrimidine: Regiochemical Parity Analysis for Exchange Behavior of Complexes between Radicals and Paramagnetic Cations

Lora M. Field,[†] Paul M. Lahti,*,[†] Fernando Palacio,[‡] and Armando Paduan-Filho[§]

*Contribution from the Department of Chemistry, University of Massachusetts,
Amherst, Massachusetts 01003, Instituto de Ciencia de Materiales de Aragón,
CSIC−Universidad de Zaragoza, 50009 Zaragoza, Spain, and
Instituto de Fisica, Universidade de São Paulo, São Paulo, Brazil*

Received January 28, 2003; E-mail: lahti@chemistry.umass.edu

Abstract: $Mn(hfac)_2$ and $Cu(hfac)_2$ form coordination complexes with 5-(4-[*N-tert*-butyl-*N*-aminoxyl]phenyl)-pyrimidine, PyrimPh-NIT. $(Mn[PyrimPh-NIT](hfac)_2)_2$ and $(Cu[PyrimPh-NIT](hfac)_2)_2$, **1** and **2**, respectively, are cyclic M_2L_2 dimers that exhibit strong exchange coupling between the coordinated paramagnetic dication (M) and nitroxide (NIT) unit. The M-NIT exchange is strongly antiferromagnetic (AFM) in **1** and strongly ferromagnetic (FM) in **2**. Magnetic susceptibility measurements for **1** were fitted to an AFM spin pairing model with $J/k = -0.25$ K between Mn-NIT spin sites units. Complex **2** also exhibits AFM spin pairing between $S = 1$ Cu-NIT spin units that is somewhat field dependent at low temperature. The fit of corrected paramagnetic susceptibility $\chi(T)$ to an AFM spin pairing model at 200 Oe yields $J/k = (-)3.8$ K, quite similar to earlier measurements at 1000 Oe yielding $J/k = (-)5.0$ K. At 1.40 K, the magnetization of **2** does not approach saturation until somewhat above 170 kOe, giving an S-shaped curve; at 0.55 K, the magnetization curve shows steps characteristic of field-induced crossover between the $S = 0$ ground state and excited spin states. From the steps in the 0.55 K data, we estimate $J/k = (-)3.8-4.0$ K for **2**, in good agreement with the analysis of $\chi(T)$.

Introduction

One very promising strategy for the design and synthesis of molecular magnetic materials is to combine paramagnetic cations with organic open-shell molecules to make hybrid systems. Nitronylnitroxides, nitroxides, and verdazyls have all been coordinated with paramagnetic ions to make hybrid materials with varying types of magnetic behavior.[1] Various qualitative models for understanding spin density distribution in organic radicals and polyradicals have been combined with overlap models incorporating the magnetic spin−orbitals of transition metals, as part of efforts to predict the magnetic behavior of the hybrid molecular magnetic materials. Such materials combine the increased magnetic moment of transition metals with the structural control of organic chemistry. A particularly useful feature of this strategy is that even antiferromagnetic (AFM) exchange coupling between transition metal and organic building block can lead to a material with a net magnetic moment, so long as the transition metal has a higher spin moment than the coordinated organic fragment.

In this article, we describe the crystallography and magnetic behavior of two coordination complexes formed between manganese(II) hexafluoroacetylacetonate/copper(II) hexafluoroacetylacetonate and the conjugated radical 5-(4-[*N-tert*-butyl-*N*-aminoxyl]phenyl)pyrimidine (PyrimPh-NIT): 1:1 cyclic, dimeric complexes[Mn(PyrimPh-NIT)(hfac)$_2$] and [Cu-(PyrimPh-NIT)(hfac)$_2$], **1** and **2**, respectively. We shall refer to these complexes as 1:1 complexes because of the ion-to-radical ratio, although they are structurally M_2L_2 type complexes. A preliminary account of some of these results has been published elsewhere.[2]

Results

Figure 1 summarizes the syntheses of complexes **1** and **2**. Silyl-protected hydroxylamine **3** was converted to boronic acid **4**, subjected to palladium-catalyzed coupling with 5-bromopyrimidine to give **5**, and deprotected to hydroxylamine **6**. The hydroxylamine was oxidized with lead dioxide to give large,

† University of Massachusetts.
‡ CSIC−Universidad de Zaragoza.
§ Universidade de São Paulo.
(1) For general references, see the following: (a) Kahn, O. *Molecular Magnetism*; VCH: New York, 1993. (b) Iwamura, H.; Inoue, K.; Hayamizu, T. *Pure Appl. Chem.* **1996**, *68*, 243. (c) Caneschi, A.; Gatteschi, D.; Sessoli, R.; Rey, P. *Acc. Chem. Res.* **1989**, *22*, 392. (d) Caneschi, A.; Gatteschi, D.; Sessoli, R. In *Magnetic Molecular Materials*; Gatteschi, D., Kahn, O., Miller, J. S., Palacio, F., Eds.; Kluwer: Dordrecht, The Netherlands, 1991; p 215. (e) Gatteschi, D.; Rey, P. In *Magnetic Properties of Organic Materials*; Lahti, P. M., Ed.; Marcel Dekker: New York, 1999. (f) Caneschi A.; Gatteschi, D.; Rey, P. In *Progress in Inorganic Chemistry*; Lippard, S. J., Ed.; Wiley: New York, 1991; Vol 39, p 331.

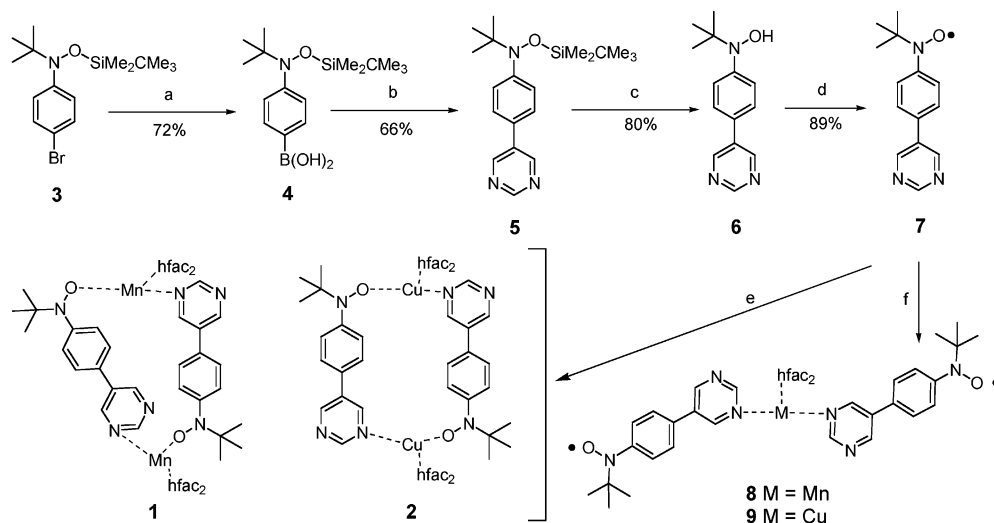(2) Field, L. M.; Lahti, P. M.; Palacio, F. *Chem. Commun.* **2002**, 636.

Figure 1. (a) *t*-BuLi, Et$_2$O, −78 °C; then B(OCHMe$_2$)$_3$; then NH$_4$Cl. (b) Pd(CH$_3$CO$_2$)$_2$, aq K$_2$CO$_3$, THF, 5-bromopyrimidine. (c) concd HCl, EtOH. (d) PbO$_2$, EtOAc. (e) Mn(hfac)$_2$·3H$_2$O, acetone or Cu(hfac)$_2$·3H$_2$O, EtOAc. (f) 0.5 equiv of Mn(hfac)$_2$·3H$_2$O, acetone or 0.5 equiv Cu(hfac)$_2$·3H$_2$O, EtOAc.
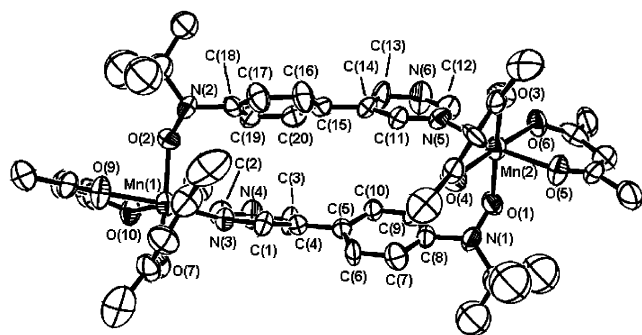

Figure 2. ORTEP diagram for complex **1**. Fluorine atoms are hidden for ease of viewing; multiple CF$_3$ groups and one *tert*-butyl group are rotationally disordered. Some atoms were not labeled for clarity of presentation; see Supporting Information for more information.

Figure 3. ORTEP diagram for complex **2**. Fluorine atoms are hidden for ease of viewing; multiple CF$_3$ groups are rotationally disordered. Some atoms were not labeled for clarity of presentation; see Supporting Information for more information.

deep-red sheets of needles of radical **7**, which is stable to ambient conditions and was readily characterized by both ESR spectroscopy and elemental analysis.

Layered 1:1 mol:mol solutions of Mn(hfac)$_2$·3H$_2$O with radical **7** crystallized slowly in air to give deep red plates of **1**. The same procedure was carried out using Cu(hfac)$_2$·3H$_2$O to give red crystals of **2**. Both **1** and **2** formed using various ratios of M(hfac)$_2$·3H$_2$O:**7** ≥ 1. When M(hfac)$_2$·3H$_2$O:**7** ≤ 0.5, 1:2 complexes **8** and **9** are formed. Details about **8** and **9** will be given elsewhere.[3] Both **1** and **2** are stable and readily characterized by spectroscopy, elemental analysis, and magnetic susceptibility. Figures 2 and 3 show crystallographic ORTEP representations of the complexes, while Table 1 lists selected structural parameters.

Discussion

Synthesis of Complexes 1 and 2. Both dimeric complexes are formed readily, so long as M(hfac)$_2$:**7** > 0.5. Upon mixing of the cation with the radical, the solution at once turns very dark (nearly opaque). UV−vis spectra of these solutions show little difference by comparison to solutions of **7** or the appropriate M(hfac)$_2$, although UV−vis of mulls of solid **1** and **2** show extra, longer wavelength bands by comparison to solid **7**. The ESR spectrum of **1** shows a somewhat distorted nitroxide
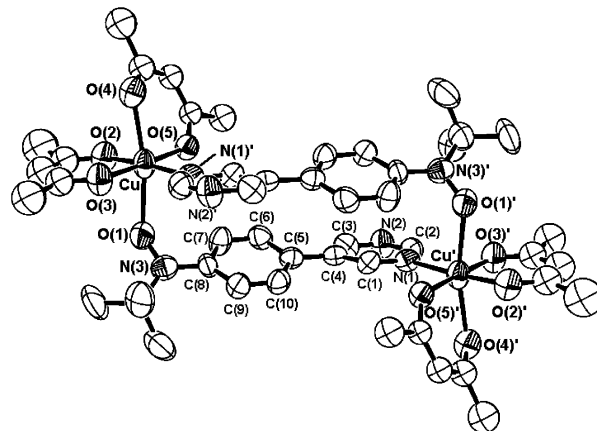
(3) Field, L. M.; Lahti, P. M.; Palacio, F.; Morón, C. Unpublished.

triplet and a variety of peaks attributable to Mn(II),[4] while that of **2** shows a more distorted nitroxide triplet and a set of peaks attributable to Cu(II).[4] The peaks are sharper in frozen solution spectra (77 K) than at room temperature for both compounds but otherwise do not change much upon cooling.

The solution spectra appear to show equilibrium mixtures of metal cations, free or partially coordinated radicals, possibly including **1** and **2** and/or **8** and **9**. The spectra do not appear sufficiently altered from individual component spectra to be due mostly to discrete molecular **1** or **2**, but there is enough spectral complexity to support some level of coordination. We consider it likely that dimers **1** and **2** are formed by reversible assembly of ions and radicals, including possible dimerization of an initial ML monomeric complex of metal cation and radical (Scheme 1).

Structure and Spin Density Considerations. Both **1** and **2** are hexacoordinate with four oxygens from two hfac groups,

(4) For the effects of coordination on ESR spectra of a number of transition metal cations, see (a) Rieger, P. H. Electron Spin Resonance Studies of Organometallic Species. In *Organometallic Processes*; Trogler, W. C., Ed.; Elsevier: Amsterdam, The Netherlands 1990; pp 270−305. (b) Bencini A.; Gatteschi, D. *EPR of Exchange Coupled Systems*; Springer-Verlag: New York, 1990.

Table 1. Selected Molecular Structure and Close Contact Parameters for 1:1 Complexes **1** and **2**[a]

r(Mn[1]−O[8]), hfac	2.119(8) Å	r(Cu−O[3]), equatorial hfac	1.933(5) Å
r(Mn[1]−O[10])	2.133(8) Å	r(Cu−O[5]), equatorial hfac	1.946(5) Å
r(Mn[1]−O[7])	2.159(9) Å	r(Cu−O[2]), equatorial hfac	1.978(6) Å
r(Mn[1]−O[9])	2.179(8) Å		
r(Mn[2]−O[4])	2.109(8) Å	r(Cu−O[4]), axial hfac	2.297(6) Å
r(Mn[2]−O[6])	2.145(8) Å		
r(Mn[2]−O[3])	2.167(8) Å		
r(Mn[2]−O[5])	2.170(8) Å		
r(Mn[2]−O[1]N), M-NIT	2.129(8) Å	r(Cu−O[1]N), axial	2.434(6) Å
r(Mn[1]−O[2]N)	2.142(9) Å		
r(Mn[2]−N[5])	2.261(9) Å	r(Cu−N[1]), equatorial	2.062(6) Å
r(Mn[1]−N[3])	2.286(9) Å		
r(Mn[1]⋯Mn[2]) intra	10.421(3) Å	r(Cu−Cu) intra	10.538(1) Å
r(Mn[1]⋯Mn[2]′) inter	6.068(3) Å	r(Cu−Cu) inter	8.191(1) Å
r(N[1]−O[1])	1.306(12) Å	r(N[1]−O[3])	1.254(9) Å
r(N[2]−O[2])	1.275(12) Å		
∠Ph−Pyrim, torsion		∠Ph−Pyrim, torsion	
C[3]−C[4]−C[5]−C[10]	28.7(17)°	C[3]−C[4]−C[5]−C[6]	24.9(10)°
C[13]−C[14]−C[15]−C[20]	32.8(17)°		
∠ON−Ph, torsion		∠ON−Ph, torsion	
O[1]−N[1]−C[8]−C[9]	39.9(15)°	C[7]−C[8]−N[3]−O[1]	27.3(10)°
O[2]−N[2]−C[18]−C[19]	45.2(15)°		
C[13]−N[6] (H-bond)	3.144(19) Å	C[2]−C[3]′ (π-stacking)	3.364(10) Å
C[20]⋯N[4] (H-bond)	3.649(18) Å		

[a] Numbering schemes given in Figures 2 and 3 and Scheme 3.

Scheme 1
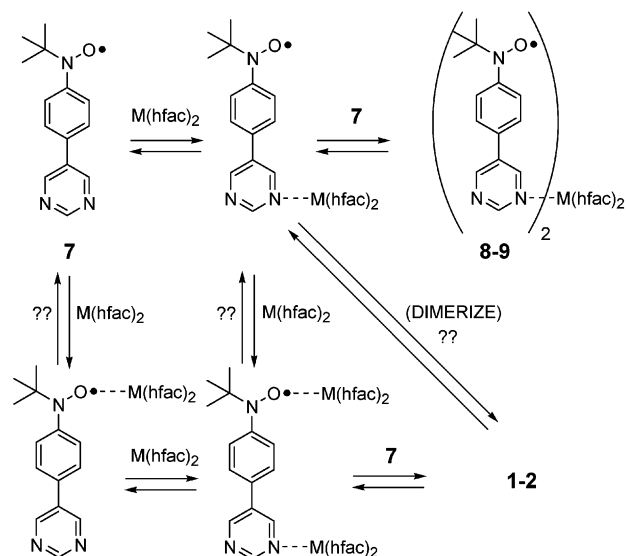
one pyrimidine nitrogen, and one nitroxide (NIT) oxygen. The CF$_3$ groups in both are disordered, as is one *tert*-butyl group in **1**. System **1** incorporates different conformations of **7**, one with a nitroxide syn to the coordinated pyrimidine nitrogen and one anti. By comparison, system **2** is centrosymmetric. The Mn−O bond length trends in **1** are not clearly differentiated, although the coordination sphere about Mn(II) is roughly octahedral. The Cu−O(NIT) bond lengths in **2** are notably longer than the other Cu−O bond lengths (Table 1), consistent with coordination of the nitroxide oxygen at a bond-elongated axial site of a distorted octahedron. In both cases, the nitroxide oxygen is coordinated anti to an hfac oxygen atom.

An important part of the initial design strategy for **1** and **2** was to use the spin density distribution in **7** to link the paramagnetic ions. Spin polarization considerations predict

negative spin density on the nitrogen atoms of the pyrimidine rings in **7**. UB3LYP/6-31G* hybrid density functional[5] model computations using Gaussian 98[6] confirm this, showing Mulliken spin populations of 9.0% and (−)4.7% on the carbons ortho and meta to the nitroxide group, but only about (−)0.5% on the pyrimidine nitrogens. Further details are given in the supporting material. These results are in excellent accord with our estimates of spin populations of 9.6% and 4.3% on the carbons ortho and meta to the nitroxide in **7**, based on the experimental aromatic proton hyperfine coupling constants a_H and using the equation $a_H = Q\rho$, where ρ is the spin density on the aromatic carbon and $Q = (−)22$ G. There is no experimentally resolvable hyperfine coupling from the pyrimidine ring. Thus, computation and experiment both suggest that **7** will have limited nitroxide to pyrimidine spin delocalization along the pathway NIT-Ph−Pyrim⋯M, where M = paramagnetic ion. However, we hoped that spin polarization (induced on the pyrimidine unit by the coordinated paramagnetic ions) would improve intramolecular exchange between the M-NIT spin units directly along a M-NIT-Ph−Pyrim⋯M-NIT pathway.

(Mn(PyrimPhNIT)hfac$_2$)$_2$, 1. We investigated the behavior of paramagnetic susceptibility (χ) versus temperature for **1**. A plot of χT versus T gives a high-temperature limit corresponding to about $S = 2.1$ with fixed $g = 2$ (Figure 4). Over the temperature range of 1.8−300 K, $1/\chi$ versus T showed linear Curie−Weiss behavior, with slope $C = 3.311$ emu·K/Oe·mol corresponding to $S = 2$ and $g = 2.12$. These results show a strong AFM exchange interaction between Mn(II) and the nitroxide unit yielding an overall $S = (^5/_2) − (^1/_2) = 2$ at room temperature. Axially coordinated nitroxide radicals tend to be AFM exchange coupled to Mn(II) in a high-spin octahedral environment, due to interactions between the radical π-SOMO and the magnetic d-orbitals on Mn(II).[1f,7]

We carried out UB3LYP/6-31G* level state energy computations on a crystallographically derived half-dimer model for **1** to compare AFM versus FM Mn(II)-NIT exchange (Figure 5). The comparison results for the model of **2** will be discussed subsequently. We adjusted[8] the computed gap for effects of spin contamination in the $S = 2$ versus the $S = 3$ state and found $\Delta E = −9$ kJ/mol, that is, favoring the low spin $S = 2$ state. The effect of spin contamination in comparing computed to experimental ΔE is not entirely clear here, but the qualitative prediction by this procedure is correct for Mn-NIT.

The limiting value of χT for **1** at higher temperatures, computed using the half-dimer molar weight, corresponds to an effective magnetization of $\mu_{eff}/\mu_B = 2.828(\chi T)^{1/2} = 7.4$ for

(5) Becke, A. D. *J. Chem. Phys.* **1993**, *98*, 5648.
(6) Frisch, M. J.; Trucks, G. W.; Schlegel, H. B.; Gill, P. M. W.; Johnson, B. G.; Robb, M. A.; Cheeseman, J. R.; Keith, T.; Petersson, G. A.; Montgomery, J. A.; Raghavachari, K.; Al-Laham, M. A.; Zakrzewski, V. G.; Ortiz, J. V.; Foresman, J. B.; Cioslowski, J.; Stefanov, B. B.; Nanayakkara, A.; Challacombe, M.; Peng, C. Y.; Ayala, P. Y.; Chen, W.; Wong, M. W.; Andres, J. L.; Replogle, E. S.; Gomperts, R.; Martin, R. L.; Fox, D. J.; Binkley, J. S.; Defrees, D. J.; Baker, J.; Stewart, J. P.; Head-Gordon, M.; Gonzalez, C.; Pople, J. A. *Gaussian 98*; Gaussian Inc.: Pittsburgh, PA, 1998.
(7) Cf. the summary and citations in ref 1f, pages 355−356.
(8) Various schemes have been proposed for correcting exchange energy gaps between high and low spin states formed by coupling of localized spin sites, for example: (a) Noodleman, L. *J. Chem. Phys.* **1981**, *74*, 5737. (b) Ruiz, E.; Cano, J.; Alvarez, S.; Alemany, P. *J. Comput. Chem.* **1999**, *20*, 1391. (c) Soda, T.; Kitagawa, Y.; Onishi, H.; Takano, Y.; Shigeta, Y.; Nagao, H.; Yoshioka, Y.; Yamaguchi, K. *Chem. Phys. Lett.* **2000**, *319*, 223. We used the method of ref 8c to make correction for the energy gaps of **1** and **2**, dividing the computed energy difference by the computed difference in ⟨S^2⟩ between the two states.
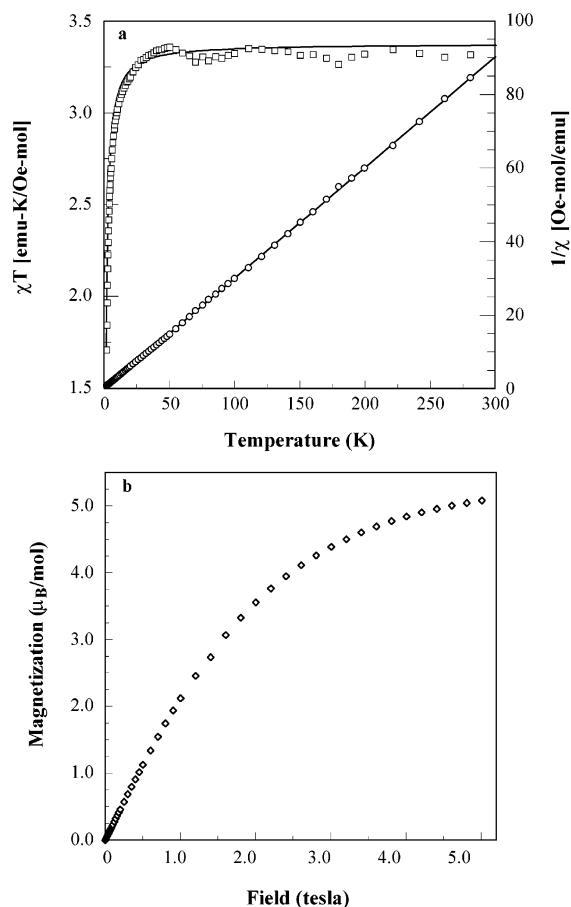
Figure 4. For complex **1**, (a) plot shows χT versus T ($\triangle$) and $1/\chi$ versus T (○), all at 1000 Oe. Solid line for χT versus T uses eq 1; solid line for $1/\chi$ versus T is a Curie−Weiss linear fit to all data. (b) Plot shows M versus H data (M = magnetization, H = field) at 1.8 K.

the full dimer. Although slightly high, this is in reasonable agreement with the value of $\mu_{eff}/\mu_B = 6.93$ expected for a system with two energetically degenerate $S = 2$ units per mole. The saturation magnetization M versus field/temperature (H/T) extrapolates to about 4.16 μ_B/mol, consistent with an $S = 2$ system having $g_{avg} = 2.1$ in the half-dimer.

The higher temperature $1/\chi$ versus T data for **1** yields[2] a Weiss constant of $\theta = -0.15$ K, showing a weak generalized AFM interaction *between* Mn-NIT spin units, despite the strong Mn-NIT AFM exchange *within* a single unit. The downturn of the χT versus T plot for **1** also shows AFM exchange coupling of spin sites at low temperature. The χT versus T for **1** was fitted to the model[9] of eq 1 for spin pairing of $S = 2$ spin units.

$$\chi = \left(\frac{N_0 g_1 g_2 \mu_B^2}{kT}\right) \cdot$$
$$\frac{84 + 6\exp(-10x) + 30\exp(-6x) + 180\exp(8x)}{7 + \exp(-12x) + 3\exp(-10x) + 5\exp(-6x) + 9\exp(8x)}$$
$$(x = J/kT)$$
$$(1)$$

Here, g_1 and g_2 are Landé constants for component spin units, k is the Boltzmann constant, μ_B is the Bohr magneton constant, and N_0 is Avogadro's number. Figure 4 compares the experi-

(9) Carlin, R. L. *Magnetochemistry*; Springer-Verlag: Berlin, Germany, 1986.

E (S=3) = -2310.532756 a.u. (<S²> =12.01)
E (S=2) = -2310.550988 a.u. (<S²> = 6.71)

E (S=0) = -2799.7926782 a.u. (<S²> = 1.01)
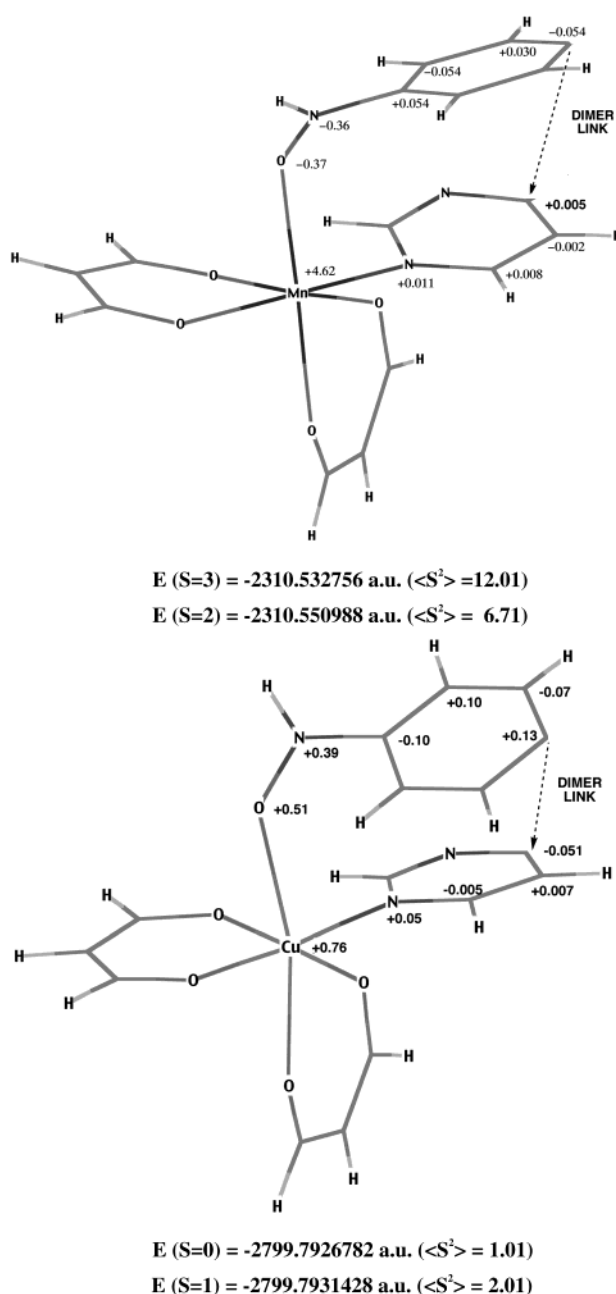E (S=1) = -2799.7931428 a.u. (<S²> = 2.01)

Figure 5. State energies for UB3LYP/6-31G* computations on half-dimer models of **1** and **2**, using the crystallographic geometries with replacement of disconnection sites by C−H bonds (not shown). Energies are given hartrees (au). Selected Mulliken spin densities are shown for the lowest energy states.
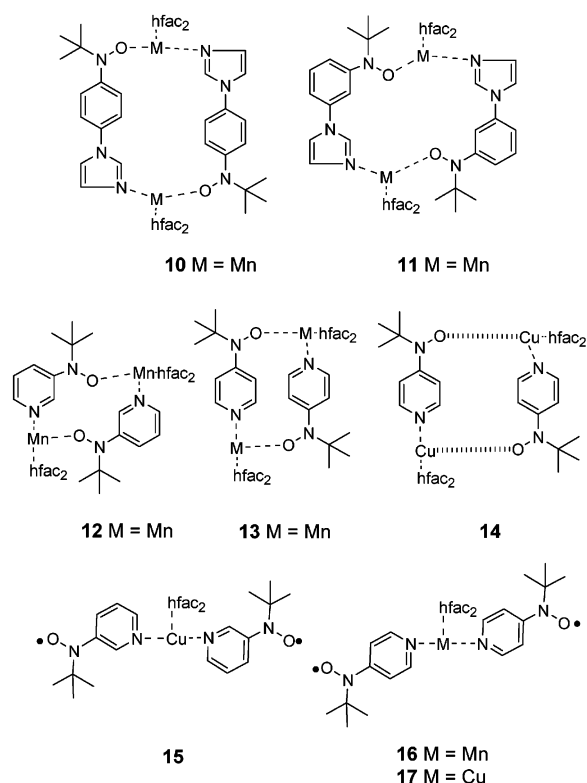
mental data to the fitted model, which gives an exchange coupling constant of $J/k = -0.25$ K for $g_1 = g_2 = 2.0$.

Iwamura and co-workers studied a set of complexes related to **1** and **2**.[10] The Mn(hfac)$_2$ 1:1 cyclic complex with *N*-(4-*tert*-butylnitroxylphenyl)imidazole, 4-NITPh-Im), **10**,[10a] shows strong Mn-NIT AFM exchange interaction, with an onset below 100 K of an FM interaction of $J/k = +0.59$ K between the $S = 2$ Mn-NIT spin sites. The connectivity isomer with 3-(4-*tert*-

(10) (a) Ishimura, Y.; Inoue, K.; Koga, N.; Iwamura, H. *Chem. Lett.* **1994**, 1693. (b) Kitano, M.; Ishimaru, Y.; Inoue, K.; Koga, N.; Iwamura, H. *Inorg. Chem.* **1994**, *33*, 6012. (c) Iwamura, H.; Koga, N. *Mol. Cryst. Liq. Cryst.* **1999**, *334*, 437. (d) See Koga, N.; Iwamura, H. In *Magnetic Properties of Organic Materials*; Lahti, P. M., Ed.; Marcel Dekker: New York, 1999; p 641. (e) Rabu, P.; Drillon, M.; Iwamura, H.; Gorlitz, G.; Itoh, T.; Matsuda, K.; Koga, N.; Inoue, K. *Eur. J. Inorg. Chem.* **2000**, 211.

Chart 1

10 M = Mn   **11** M = Mn

12 M = Mn   **13** M = Mn   **14**

15   **16** M = Mn
                17 M = Cu

Scheme 2

1   **2**

10   **13**

Scheme 3

1

butylnitroxylphenyl)imidazole (3-NITPh-Im), **11**, shows AFM exchange behavior between the $S = 2$ units with $J/k = -0.22$ K. The difference was attributed to different regiochemical connectivities of the complexes, although it was not clear whether the effects in **10** and **11** were purely intramolecular. Complex **12**, a connectivity analogue of **1** with 3-pyrimidyl-*tert*-butylnitroxide (3-NIT-Py), has not been described to our knowledge. But, the known para complex **13**[10b,e] with 4-pyrimidyl-*tert*-butylnitroxide (4-NIT-Py) exhibits strong AFM exchange within an Mn-NIT spin unit ($S = 2$) and moderate FM exchange[10e] of $J/k = +8.7$ K between units. The stronger exchange in **13** by comparison to **10** and **11** is probably due to a smaller number of bonds in the intramolecular exchange pathway (Chart 1).

In the absence of **12**, complexes **10** and **13** seem to be the best benchmarks for the behavior of **1**. Kitano et al.[10b] described the spin polarization pathways expected in π-conjugated nitroxides coordinated to Mn(II). Their model is consistent with the FM exchange observed[10e] between Mn-NIT spin sites in **13**. Extrapolating, the Mn-NIT spin sites should be intramolecularly AFM exchange coupled in **1**, as shown in Scheme 2 and consistent with the observed behavior.

The comparison of **1** to **10** (or **11**) is less straightforward. The imidazole rings in **10** and **11** introduce nonalternant effects into the spin-density distribution. Although **10** is structurally similar to **1** (Scheme 2), **10** exhibits FM exchange between Mn-NIT spin units, the qualitative reverse of **1**. UB3LYP/6-31G* model spin density computations on the organic radical portion of **10** show a small positive spin density on the coordinating imidazole nitrogen, +0.35% (see Supporting Information for further details). Interannular delocalization in **10** is thus quite limited, as in radical **7**. But, the positive spin polarization on the coordinating imidazole nitrogen, opposite to the negative
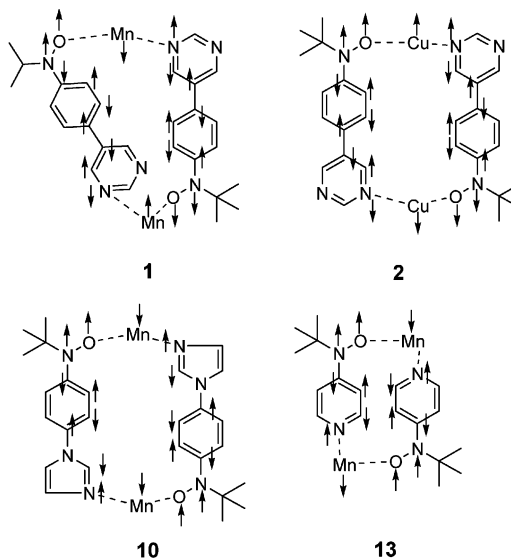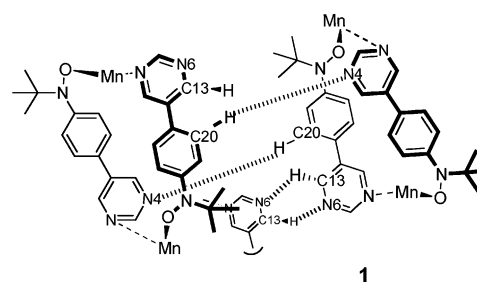
sign of the spin density on the coordinating nitrogen of radical **7**, is consistent with the reversal of qualitative exchange behavior between **10** and **1**.

We considered the possibility that through-space interaction between Mn-NIT spin sites could account for the small exchange couplings observed for **1** and **10**. In **1**, the intramolecular and closest intermolecular Mn···Mn distances are 10.42 and 6.07 Å, respectively. The corresponding distances in **10** are 10.65 and 8.21 Å. If intermolecular Mn···Mn distances alone controlled exchange in **10**, even stronger effects would seem likely in **1** due to the closer contacts. So simplistic an argument would not, of course, account for differences in orbital overlap for different geometries.

We also considered possible intermolecular exchange by spin polarization through close atomic contacts. The closest interdimer contacts in **1** are hydrogen-bond type interactions formed by complementary C−H···N interactions between pyrimidine rings (Scheme 3, C20−H···N4). The very small spin densities on the pyrimidine ring suggest this to be a very weak exchange mechanism. Although the observed exchange between Mn-NIT spin sites is quite weak, the model of Scheme 3 also suggests a qualitatively FM exchange linkage, opposite to the observed behavior. No other intermolecular close-contact pathways linking Mn-NIT spin sites in **1** seem likely to cause AFM exchange.

Thus, the AFM exchange in **1** is consistent with spin polarization models[10] for through-bond coupling of the Mn-NIT spin units in **10** and **11** and **13**. Because of the weakness of the exchange, it is difficult to ascribe it definitively to an intramolecular spin polarization mechanism. Nonetheless, there are no clear intermolecular pathways that clearly fit the
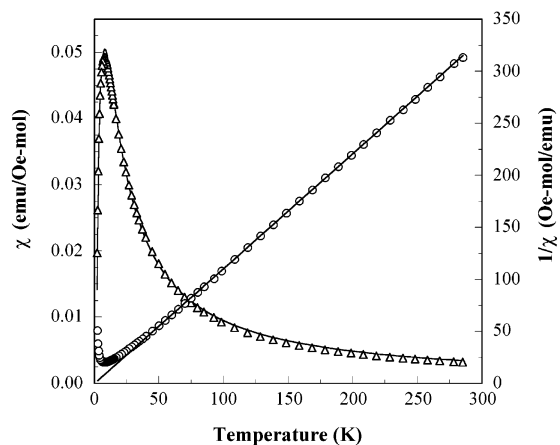
Figure 6. For complex **2**, the plot shows χ versus T ($\triangle$) and $1/\chi$ versus T ($\bigcirc$), at 200 Oe. Solid lines for χ versus T uses eq 3; solid line for $1/\chi$ versus T is a Curie–Weiss linear fit to the data for $T > 150$ K.
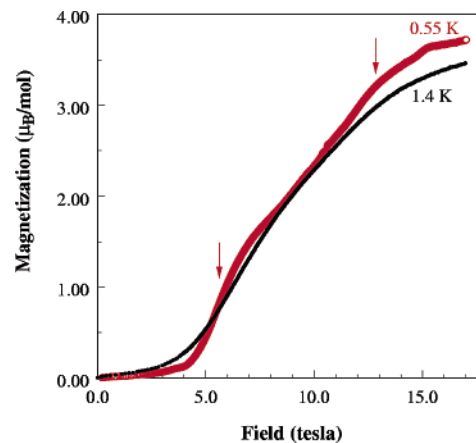

Figure 7. Magnetization versus field, H, isotherms at 0.55 K (red) and 1.4 K (black). Arrows show positions of spin state level crossing steps described in the text.

qualitative exchange behavior. Given the consistency of our results with models for the behavior of previously studied **10**, **11**, and **13**, we feel that use of the spin polarization mechanism is justified as a working model for all of these systems.

(Cu(PyrimPhNO)hfac₂)₂, 2. A $1/\chi$ versus T plot at 200 Oe for **2** yields a Curie constant of $C = 0.909$ emu K/Oe mol and a Weiss constant of $\theta = -0.2$ K (Figure 6). The Curie constant corresponds to $S = 0.94$ if $g = 2$. Thus, **2** exhibits strong FM interaction between the Cu(II) ions and the nitroxide units, with effective $S = 1$. High temperature values of χT versus T approach an equivalent magnetization value of $\mu_{eff}/\mu_B \cong 4.0$, in good agreement with the value of 4.00 expected for a molecule composed with two $S = 1$ Cu-NIT units.

We carried out UB3LYP/6-31G* computations on a crystallographically derived half-dimer model of **2**. Figure 5 shows computed energies for the $S = 0$ and $S = 1$ states of the model, as well as the Mulliken spin density populations in the high spin state. The high spin state is favored by $\Delta E = 1.7$ kJ/mol when the computed energies are adjusted using eq 1. The favoring of a high spin state for Cu(II)-NIT in axial coordination been explained elsewhere in terms of orthogonality between the SOMO's of Cu(II) and the nitroxide.[1f,11−12] The results of Figure 5 are best considered a qualitative comparison to experiment, but the computed high spin state is correctly favored in **2**.

The χ versus T plot for **2** maximizes at 8 K and then decreases rapidly down to the minimum measurement temperature. This is indicative of antiferromagnetic spin pairing between $S = 1$ units, for which the Hamiltonian is given by eq 2,

$$\mathscr{H} = -2J\,\mathbf{S}_1 \cdot \mathbf{S}_2 + g\mu_B H\,(S_{1z} + S_{2z}) \quad (2)$$

This Hamiltonian is diagonal in the magnitude S_T of the total spin of the pair and in the projection m of the total spin $\mathbf{S}_T$ along $\mathbf{H}$. The energy levels can be obtained by noting that $\mathbf{S}_T = \mathbf{S}_1 + \mathbf{S}_2$ obeys the relation given by eq 3,

$$\mathbf{S}_T \cdot \mathbf{S}_T = \mathbf{S}_1 \cdot \mathbf{S}_1 + \mathbf{S}_2 \cdot \mathbf{S}_2 + 2\mathbf{S}_1 \cdot \mathbf{S}_2 \quad (3)$$

Since $\mathbf{S}_1 = \mathbf{S}_2 = \mathbf{S}$, this leads to a set of energies given by eq 4,

$$E = \langle S_T m | \mathscr{H} | S_T m \rangle =$$
$$-J[S_T(S_T + 1) - 2S(S + 1)] + g\mu_B mH \quad (4)$$

Accordingly, the ground state of **2** will be $S_T = 0$, while $S_T = 1$ and $S_T = 2$ will be excited state spin levels at energetic spacings of $2J$ and $6J$, respectively.

The χ versus T data was fitted to the above spin-pairing model,[9] with incorporation of an additional mean field interaction term. Equation 5 gives the expression for the temperature dependence of the susceptibility: the constants have the same meanings as given for eq 1 earlier, with the addition of θ as the mean-field term.

$$\chi = \left(\frac{N_0 g_1 g_2 \mu_B{}^2}{k(T - \theta)}\right) \frac{\exp(2x) + 5\exp(6x)}{1 + 3\exp(2x) + 5\exp(6x)} \quad (5)$$

$$(x = J/kT)$$

The behavior is slightly field dependent. We previously described[2] a preliminary study of **2** at 1000 Oe, from which we found $J/k = -5.0$ K, $\theta = -1.1$ K, using fixed values of $g_1 = 2.00$ and $g_2 = 2.20$. By comparison, fitting of the data at 200 Oe gives $J/k = -3.79$ K, using fixed values of $g_1 = g_2 = 2.00$ and $\theta = -0.2$ K (Figure 6). Overall, **2** exhibits stronger AFM exchange coupling between M-NIT spin units than **1** under all conditions tested.

The magnetization versus field plot does not saturate up to 50 kOe; instead, it increases smoothly and exhibits a shape that strongly differs from a Brillouin function. However, magnetization experiments made at higher fields show an S-shaped behavior, as shown for measurements made at 1.4 and 0.55 K in Figure 7. The shape is very smooth in the 1.4 K isotherm, whereas at 0.55 K a clear "ripple" is observed. In the latter plot, over 0−40 kOe, the magnetization is quite small and increases very slowly, but at higher fields, it rapidly increases to form a shoulder at approximately $2\mu_B$ corresponding to the $S = 1$ state. Increasing the magnetic field further gives another rapid increase in magnetization and a second shoulder at approximately $4\mu_B$ corresponding to the $S = 2$ spin state. The width of these transitions is independent of the applied magnetic field.

This magnetization behavior strongly supports the spin pairing model used to model the temperature dependence of the susceptibility. The shoulders observed in the 0.55 K magnetization isotherm originate from crossovers of higher spin multiplets at larger applied fields. At zero-field, the $|S_T = 0, M = 0\rangle$ state
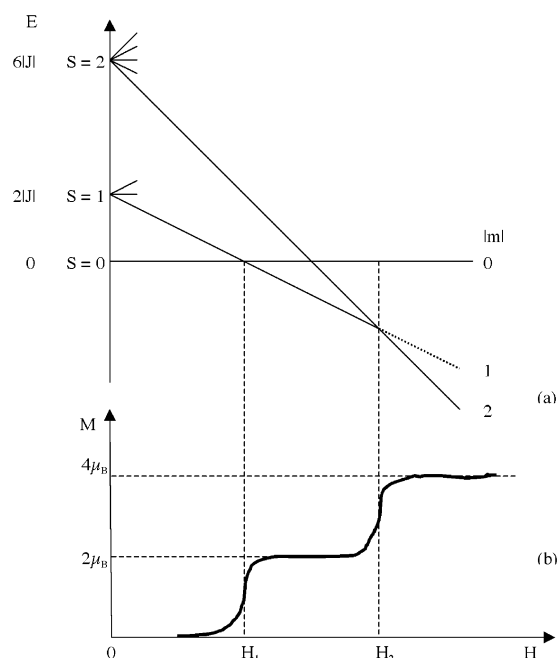
Figure 8. (a) Energy level diagram for the pair model (see text) and Zeeman splitting of these levels in a magnetic field H. Note that the crossing of levels at H_1 and H_2 changes the ground state. (b) Schematic magnetization curve at very low temperature showing the steps in the magnetization due to the successive increases of $|m|$ in the ground state before reaching real saturation.

is lowest in energy. Under application of a magnetic field, the upper spin states undergo Zeeman splitting, as shown in Figure 8a. Only the $S_T = 0$ zero-field ground state level is not split. Due to the Zeeman splitting, the ground state of the overall dimer **2** changes with increasing H. Thus, as the magnetic field is increased, the $|S_T = 1, m = -1\rangle$ energy level from the $S_T = 1$ manifold drops in energy according to $-g\mu_B H$, becoming the ground state at H_1. Because of the jump in $|m|$ at this point, the low temperature magnetization exhibits a step at H_1. Further increase of the field results in a second crossover at H_2 between the $|1, -1\rangle$ and the $|2, -2\rangle$ spin states; the latter becomes the ground state, and so the magnetization $|m|$ again increases by one unit. Since this is the highest spin value of the pair, the magnetization will saturate at sufficient high field. These steps in the magnetization are sketched qualitatively in Figure 8b. If the temperature is sufficiently low compared to $|J/k|$, the steps and subsequent saturation plateaus in the magnetization can be clearly observed. However, as T approaches the value of $|J/k|$, thermal population obscures the steps, and the magnetization appears to increase smoothly up to the saturation limit. Just such behaviors are observed for the magnetization plots of Figure 7 at 0.55 and 1.4 K, respectively.

According to this model the magnetic fields at the centers of the magnetization steps are given by eq 5,

$$g\mu_B H_n = 2|J|n \qquad (5)$$

where $n = 1, 2$. Based on the data of Figure 7, we used $H_1 = 57$ kOe and $H_2 = 120$ kOe. Assuming $g = 2.0$, one obtains $|J/k|$ values for the two steps of 3.8 and 4.0 K, respectively, in excellent agreement with the fit of the susceptibility at low field in Figure 6.

There is a dearth of structural analogues to which to compare the behavior of **2**. Cu(II)-based versions Mn(II)-based **10−12**

seem not to have been described. Complex **14**[13] is a parity relative of **2** but has such long Cu−O(NIT) bonds (2.79 Å, versus 2.43 Å in **2**) that Cu(II) occupies a square-pyramidal, pentacoordinate environment, quite different from the Cu(II) environment in **2**. Iwamura and co-workers studied 1:2 complexes **15−17** related to **8** and **9**,[10b−d,13] but these do not incorporate direct Cu-NIT bonding. The following trends were described in the latter studies: (1) exchange constants J/k in the Cu(II) complexes were stronger than in the analogous Mn-(II) complexes, (2) exchange behavior seemed to be of opposite sign to that in the Mn(II) structural analogues, and (3) the spin density of the coordinated pyridine nitrogen atoms in **15** and **17** was proposed to be polarized to the same sign as the Cu(II). We tried to compare these trends to the behavior of **2**.

Scheme 2 postulates spin polarization exchange pathways for **1** and **2**. A positive spin polarization on the Cu(II)-coordinated pyrimidine nitrogen is important to yield a qualitative result, wherein both **1** and **2** are AFM coupled. The computations summarized in Figure 5 are consistent with the proposed Cu-(II)-pyrimdine spin polarization pattern. The same parity was also computed for Mn(II)-pyrimidine polarization in **1**, against the Scheme 2 proposal, but the significant $S = 3$ state contamination in the $S = 2$ computation for **1** may effect this result. The high spin $S = 1$ state of the model for **2** is not significantly spin contaminated, so we deem the spin density results for $S = 1$ Cu-NIT to be more reliable for comparison to experiment.

Overall, therefore, the intramolecular spin polarization model of Scheme 2 is plausible to explain comparative magnetic behaviors of **1** and **2** (with a caveat described in the subsequent paragraph). If we accept that this model governs their exchange natures, our experimental results clarify a structure-property deficit left by the absence of systems such as **12** and analogues summarized in Table 2.

One ambiguity in a connectivity-based analysis for **2** is the strong intermolecular overlap between π-stacked pyrimidine rings in adjacent molecules (Figure 9). No similar contact is present in **1**. Pyrimidine rings in adjacent molecules of **2** are stacked in a parallel, offset manner, only 3.364 Å apart. At this distance, the π-clouds are in direct contact. The strong overlap between sites of opposite spin density could provide an AFM exchange pathway.[14,15] Although DFT computations on **7** and on the model for **2** (Figure 5) show <2% spin densities on the pyrimidine ring, the net through-space effect might occur due to the close stacking despite the small spin overlap involved. Qualitatively, spin-pairing interaction in **2** thus might occur by

(11) For example, see: (a) Laugier, J.; Ramasseul, R.; Rey, P.; Espie, J. C.; Rassat, A. *Nouv. J. Chim.* **1980**, *7*, 11. (b) Anderson, O. P.; Kuechler, T. C. *Inorg. Chem.* **1980**, *19*, 1417. (c) Grand, A.; Rey, P.; Subra, R. *Inorg. Chem.* **1983**, *22*, 391.
(12) For some cases of AFM CuNIT exchange, see: (a) Lim, Y. Y.; Drago, R. S. *Inorg. Chem.* **1972**, *11*, 1134. (b) Porder, L. C.; Dickman, M. H.; Doedens, R. J. *Inorg. Chem.* **1985**, *24*, 1006. (c) Luneau, D.; Rey, P.; Laugier, J.; Fries, P.; Caneschi, A.; Gatteschi, D.; Sessoli, R. *J. Am. Chem. Soc.* **1991**, *113*, 124.
(13) Ishimaru, Y.; Kitano, M.; Kumada, H.; Koga, N.; Iwamura, H. *Inorg. Chem.* **1998**, *37*, 2273.
(14) McConnell, H. M. *J. Chem. Phys.* **1963**, *39*, 1910.
(15) (a) Kawakami, T.; Yamanaka, S.; Mori, W.; Yamaguchi, K.; Kajiwara, A.; Kamachi, M. *Chem. Phys. Lett.* **1995**, *235*, 257. (b) Yamaguchi, K.; Kawakami, T.; Oda, A.; Yoshioka, Y. In *Magnetic Properties of Organic Materials*; Lahti, P. M., Ed.; Marcel Dekker: New York, 1999 and references therein. (c) Yoshiozawa, K.; Hoffmann, R. *J. Am. Chem. Soc.* **1995**, *117*, 6921. (d) Yoshiozawa, K. In *Magnetic Properties of Organic Materials*; Lahti, P. M., Ed.; Marcel Dekker: New York, 1999 and references therein.

Table 2. Comparison of Exchange Behavior as a Function of Structure in Metal−Radical Complexes^a

complex	J/k (M-NIT)	J/k (S–S)	reference
[Mn(3-NITPh-Im)(hfac)$_2$]$_2$, **11**	strong, AFM at 300 K	AFM −0.22 K (S = 2)	10a
[Mn(4-NITPh-Im)(hfac)$_2$]$_2$, **10**	strong, AFM at 300 K	FM +0.59 K (S = 2)	10a
[Mn(PyrimPhNIT)(hfac)$_2$]$_2$, **1**	**strong, AFM at 300 K**	**AFM −0.25 K (S = 2)**	**This work**
[Mn(4-NIT-Py)(hfac)$_2$]$_2$, **13**	strong, AFM at 300 K	FM +8.7 K (S = 2)	10e
[Cu(PyrimPhNIT)(hfac)$_2$]$_2$, **2**	**strong, FM at 300 K**	**AFM −3.8 K (S = 1)**	**This work**
Cu(4-NIT-Py)(hfac)$_2$, **14**		FM +58.6 K	13
		(2 × S = $^1/_2$)	

^{a} J(M-NIT) shows exchange from metal cation to nitroxide (M−ON), while J/k (S−S) shows exchange between M-NIT spin units, except for **14**, where the exchange model used treats the Cu(II) and NIT spins separately.
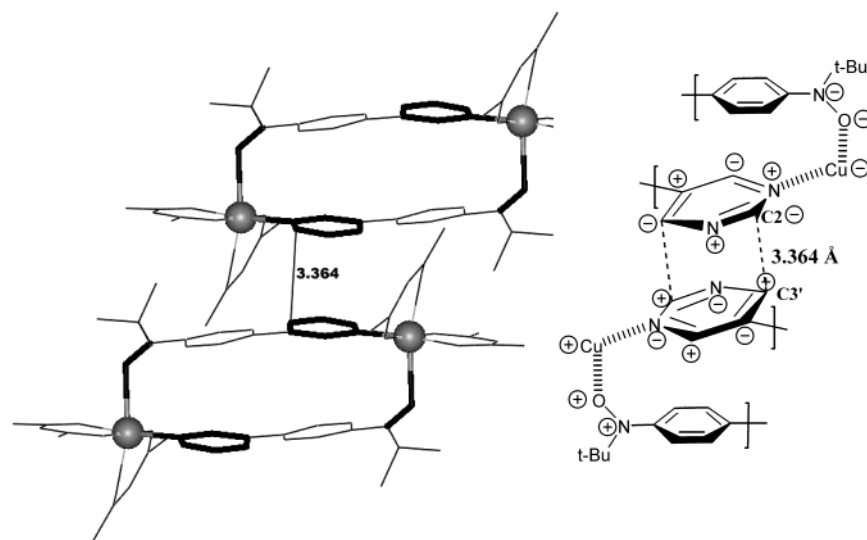

Figure 9. π-Stacking interaction between pyrimidine rings in different molecules of **2**. Ball-and-stick atoms show the interaction paths between Cu-NIT spin sites on the left-hand side of the figure. The right-hand side of the figure shows qualitative, relative spin density, based on a qualitative polarization model for AFM exchange.

a [Cu-NIT]-Pyrim·····Pyrim-[Cu-NIT] through-space interdimer overlap mechanism rather than by a spin polarization pathway between Cu-NIT sites within the cyclic dimer.

Conclusions

Mn(hfac)$_2$ and Cu(hfac)$_2$ both form cyclic, dimeric 1:1 complexes with 5-(4-[N-tert-butyl-N-aminoxyl]phenyl)pyrimidine that incorporate both metal-nitroxide and metal-pyrimidine coordination sites. Both have the same head-to-head cyclic dimer connectivity, despite the geometric differences that break the symmetry in **1** by comparison to the centrosymmetry in **2**. These systems provide information about the little-known 1:1 complexes of paramagnetic dications with meta connectivity organic radicals, models for hybrid inorganic−organic exchange-linked systems. The Mn-NIT unit is strongly and antiferromagnetically coupled (S = 2), while the axial Cu-NIT unit is strongly and ferromagnetically coupled (S = 1); for both, this behavior is observed even at room temperature.

The AFM interaction in **1** is consistent with an intramolecular spin parity analysis, although the weakness of the exchange makes it hard to rule out an intermolecular contribution conclusively. The AFM exchange in **2** is also consistent with intramolecular spin parity analysis, although this situation is complicated by a favorable interdimer π-overlap. The close intermolecular π-stacking in **2** could give AFM exchange and confuse the intramolecular spin parity analysis. It is therefore difficult to decide conclusively whether the interdimer or the intradimer exchange pathway is dominant; there even may be some contribution from both, whichever dominates. Despite this complexity, we must note that the exchange coupling of and between M-NIT spin sites in **1** and **2** is quite consistent with the qualitative, parity-based intramolecular spin parity models. These models remain convenient paradigms to design hybrid inorganic/organic magnetic materials. Unless clearly contradicted, the models are the most consistent means by which to try to predict and explain the behavior of **1** and **2** and related systems. By correlating the relative strength of exchange interactions as a function of structure, researchers will hopefully be better able to design hybrid magnetic materials from first principles.

Experimental Section

General. Diethyl ether and tetrahydrofuran (THF) were distilled under argon from sodium. N,N-Dimethylformamide (DMF) was dried over anhydrous magnesium sulfate. tert-Butyllithium in pentane and n-butyllithium in hexanes were obtained from Acros. tert-Butyldimethyl chlorosilane was obtained from Alfa Aesar. All other chemicals were obtained from Aldrich and used as received. All melting points are uncorrected.

X-ray crystallographic analyses were carried out by Dr. A. Chandrasekaran at the X-ray Structural Characterization Facility at the University of Massachusetts-Amherst. Elemental analysis was carried out by Dr. G. Dabkowski of the University of Massachusetts-Amherst Microanalysis Laboratory. NMR spectra were obtained on Bruker EMX-200 FT-NMR spectrometers. UV−vis spectra were obtained on a Shimadzu UV-260 spectrometer.

***tert*-Butyl(4-bromophenyl)-*tert*-butyldimethylsiloxylamine (3).** This compound was synthesized in 74% yield by the method of Inoue and Iwamura.[16] See Supporting Information for details.

4-(*N*-*tert*-Butyl-*N*-[*tert*-butyldimethylsiloxyl]amino)phenyl Boronic Acid (4). This compound was synthesized following the procedures of Inoue and Iwamura and of Lahti et al.[17] See Supporting Information for details.

5-[4-(*N*-*tert*-Butyl-*N*-[*tert*-butyldimethylsiloxyl]amino)phenyl]-pyrimidine (5). A flask containing 0.38 g (2.38 mmol) of 5-bromopy-rimidine and 0.027 g (0.12 mmol) of palladium acetate was evacuated and recharged with argon twice. Then, 10 mL of THF was added, and the solution was allowed to stir for 10 min. Deaerated solutions of 1.0 g (3.09 mmol) of **4** in 5 mL of THF and 0.82 g (5.95 mmol) of potassium carbonate in 4.5 mL of water were then added. The reaction was then heated to reflux and allowed to stir under argon for 1 day. The aqueous layer was then separated and extracted with diethyl ether. The combined organic layers were washed with brine, dried over magnesium sulfate, filtered, and concentrated in vacuo. The crude material was purified by chromatography on silica gel with a 2:8 mixture of ethyl acetate/hexanes to give a yellow solid product: 0.57 g, 66%, mp 73−74 °C. ^{1}H NMR (CDCl$_3$): δ −0.10 (broad s, 6 H), 0.93 (s, 9H), 1.13 (s, 9 H), 7.38 (d, 2 H, $J = 8$ Hz), 7.47 (d, 2 H, $J = 8$ Hz), 8.96 (s, 2 H), 9.17 (s, 1 H). Anal. Calcd for C$_{20}$H$_{31}$N$_3$OSi: C, 67.18; H, 8.74; N, 11.75. Found: C, 67.65; H, 9.03; N, 11.72.

5-[4-(*N*-*tert*-Butyl-*N*-hydroxylamino)phenyl]pyrimidine (6). To a solution of 0.182 g (0.509 mmol) of **5** in 5 mL of ethanol was added 1 mL of concentrated HCl. The resulting solution was allowed to stir overnight under argon. The solution was concentrated, then diluted with 5 mL water, neutralized to pH 5 with 1 M sodium hydroxide, and then extracted with dichloromethane repeatedly. The organic layers were combined, washed with water and then brine, dried over magnesium sulfate, filtered, and concentrated in vacuo to give an oil. Pale yellow, square crystals of the product formed upon recrystallization from ethyl acetate/hexane: 0.99 g, 80%, mp 142−145 °C. ^{1}H NMR (CDCl$_3$): δ −1.52 (s, 9 H), 7.66 (d, 2 H, $J = 8$ Hz), 8.02 (d, 2 H, $J = 8$ Hz), 8.97 (s, 2 H), 9.26 (s, 1 H). Anal. Calcd for C$_{14}$H$_{17}$N$_3$O: C, 69.11; H, 7.04; N, 17.27. Found: C, 68.95; H, 7.24; N, 17.21.

5-(4-*N*-*tert*-Butyl-*N*-aminoxylphenyl)pyrimidine (7). To a solution of 0.84 g (0.37 mmol) of **6** in 5 mL of ethyl acetate was added 0.090 g (0.37 mmol) of lead dioxide. The resulting suspension was allowed to stir for 2 h under argon. The suspension was then filtered through Celite, and the filtrate was allowed to slowly evaporate under air to give red crystals 0.080 g (89%) with mp 103−105 °C. Anal. Calcd for C$_{14}$H$_{16}$N$_3$O: C, 69.40; H, 6.65; N, 17.34. Found: C, 69.50; H, 6.78; N, 17.45. ESR (benzene): $g = 2.0066$, $a_N = 11.70$ (nitroxide N), $a_H = 2.11$ and 0.94 G. UV−vis (λ_{max}, tetrahydrofuran; nm[M^{-1} cm^{-1}]): 319 [37 000], 500 [5400].

[Mn(hfac)$_2$(PhPyrim-NIT)]$_2$ (1). Over a solution of 0.053 g (0.22 mmol) of **7** in 8 mL of ethyl acetate, a solution of 0.10 g (0.22 mmol) of Mn(hfac)$_2$·3H$_2$O in 0.1 mL of acetone and 8 mL of hexane was layered on top. The resulting layered solution was allowed to stand for 1 day and then allowed to evaporate for another day to give a crude solid. This solid was recrystallized from ether and hexane to give 0.064 g (41%) of dark red plates with mp 142−143 °C. UV−vis (λ_{max}, tetrahydrofuran; nm[M^{-1} cm^{-1}]): 313 [73 000], 500 [6800]. Anal. Calcd for C$_{24}$H$_{18}$N$_3$O$_5$F$_{12}$Mn: C, 40.04; H, 2.52; N, 5.84. Found: C, 40.28; H, 2.63; N, 5.64. Monoclinic space group $P2_1/c$ (#14), with $a = 9.888$-(9) Å, $b = 28.922(5)$ Å, $c = 21.273(1)$ Å, $\beta = 78.339(7)°$, $V = 5958.8$-

(2) Å^3, $Z = 4$, $D_{calc} = 1.585$ g/cm^3; 6164 unique reflections with $I > 2\sigma(I)$ were modeled with 511 variables to yield the structure with $R = 0.1341$, $wR = 0.3377$. The large R-value is due to rotational disorder in half of the CF$_3$ groups and one *tert*-butyl group.

[Cu(hfac)$_2$(PhPyrim-NIT)]$_2$ (2). Atop a solution of 0.053 g (0.22 mmol) of **7** in 8 mL of ethyl acetate was layered a second solution of 0.11 g (0.22 mmol) of Cu(hfac)$_2$·3H$_2$O in 0.1 mL of acetone and 8 mL of hexane. The resulting solution was allowed to stand for 1 day and then to evaporate slowly for another day to give a crude solid. This solid was then recrystallized from dichloromethane and hexane to give 0.084 g (54%) of red, square platelike crystals with mp 132−134 °C. Anal. Calcd for C$_{24}$H$_{18}$N$_3$O$_5$F$_{12}$Cu: C, 40.52; H, 2.55; N, 5.91. Found: C, 40.65; H, 2.48; N, 5.88. UV−vis (λ_{max}, tetrahydrofuran; nm[M^{-1} cm^{-1}]): 314 [62 000], 500 [12 000]. Monoclinic space group $C2/c$ (#15), with $a = 13.500(2)$ Å, $b = 14.53(7)$ Å, $c = 33.696(2)$ Å, $\beta = 101.02(9)°$, $V = 6485.91(16)$ Å^3, $Z = 4$, $D_{calc} = 1.475$ g/cm^3; 5710 unique reflections with $I > 2\sigma(I)$ were modeled using 382 variables to yield the structure with R = 0.1280, wR = 0.3634. The large R-value is due in part to rotational disorder in multiple CF$_3$ groups.

Magnetic Measurements. DC magnetic susceptibility experiments were carried out on two Quantum Design MPMS SQUID magnetometers in Zaragoza and in São Paulo. The samples were packed into gelatin capsules with cotton, subjected to at least 3-fold helium purge. Molar paramagnetic susceptibilities were determined after correction for diamagnetic and temperature independent contributions. Diamagnetic contributions to total susceptibility were computed using Pascal's tables. Magnetization versus field strength measurements between 0 and 50 kOe were also carried out in a Quantum Design MPMS magnetometer at 1.8 and 3 K. A vibrating sample magnetometer (VSM) was used for high-field magnetization measurements up to 17 T, which were carried out at 1.4 and 0.55 K. (In ref 2, a preliminary description of the magnetic analysis for **2** was done using eq 1 listed in this article, but the equation was incorrectly shown in that reference. The exchange constant J/k of **2** in ref 2 thus is given correctly.)

Supporting Information Available: Crystallographic summaries for **1** and **2**, summaries of DFT computations for models of **1**, **2**, and **7**, ESR spectra for **1** and **2** (fluid and frozen solutions) and **7** (fluid solution). This material is available free of charge via the Internet at http://pubs.acs.org.

JA0343813

(16) Inoue, K.; Iwamura, H. *Angew. Chem., Int. Ed. Engl.* **1995**, *34*, 927.
(17) Lahti, P. M.; Liao, Y.; Julier, M.; Palacio, F. *Synth. Met.* **2001**, *122*, 485.